catalysts

MDPI

Article

Insights into the Capture of CO_2 by Nickel Hydride Complexes

Min Zhang [1], Xiaoqing Liang [1], Yaozheng Wang [2], Hongyu Yang [3] and Guangchao Liang [3,*]

[1] Department of Pharmacy, School of Medicine, Xi'an International University, Xi'an 710077, China; zhangmin01@xaiu.edu.cn (M.Z.); xiaoqing870406@163.com (X.L.)
[2] College of Information Management, Minnan University of Science and Technology, Quanzhou 362700, China; yzwang20@outlook.com
[3] Academy of Advanced Interdisciplinary Research, Xidian University, Xi'an 710071, China; yanghongyu@xidian.edu.cn
* Correspondence: liangguangchao@xidian.edu.cn

Abstract: As a desired feedstock for sustainable energy source and for chemical synthesis, the capture and utilization of CO_2 have attracted chemists' continuous efforts. The homogeneous CO_2 insertion into a nickel hydride complex to generate formate provides insight into the role of hydrogen as an active hydride form in the hydrogenation of CO_2, which serves as a practicable approach for CO_2 utilization. To parameterize the activities and to model the structure–activity relationship in the CO_2 insertion into nickel hydride, the comprehensive mechanism of CO_2 insertion into a series of square planar transition metal hydride (TM–H, TM = Ni, Pd, and Co) complexes was investigated using density functional theory (DFT) computations. The stepwise pathway with the TM-(H)-formate intermediate for the CO_2 insertion into all seven square planar transition metal hydride (TM–H) complexes was observed. The overall rate-determining step (RDS) was the nucleophilic attraction of the terminal O atom on the Ni center in Ni-(H)-formate to form Ni-(O)-(*exo*)formate. The charge of the Ni atom in the axially vacant $[Ni]^+$ complex was demonstrated as the dominant factor in CO_2 insertion, which had an excellent linear correction ($R^2 = 0.967$) with the Gibbs barrier ($\Delta G^{\ddagger}$) of the RDS. The parameterized activities and modeled structure–activity relationship provided here light the way to the design of a more efficient Ni–H complex in the capture and utilization of CO_2.

Keywords: nickel hydride; CO_2 insertion; catalyst design; DFT

Citation: Zhang, M.; Liang, X.; Wang, Y.; Yang, H.; Liang, G. Insights into the Capture of CO_2 by Nickel Hydride Complexes. *Catalysts* **2022**, *12*, 790. https://doi.org/10.3390/catal12070790

Academic Editor: C. Heath Turner

Received: 24 June 2022
Accepted: 14 July 2022
Published: 19 July 2022

1. Introduction

The utilization of CO_2 as the sustainable carbon feedstock for energy source and for chemical synthesis has been demonstrated as a promising strategy in solving the environmental crisis caused by the consumption of fossil fuels [1–4]. The well-developed approaches for the capture and utilization of CO_2 including the reduction of CO_2 [5,6] and hydrogenation of CO_2 [7–9] have been established. The transition metal (TM) complex-catalyzed homogeneous hydrogenation of CO_2 to formate usually involves (1) activation of a H_2 molecule to form the hydride species, (2) CO_2 insertion into the TM–H bond, and (3) the release of formate and regeneration of the catalyst. As a critical step in the catalytic hydrogenation of CO_2 to formate, the capture of CO_2 by transition metal hydride complex (TM–H) via the CO_2 insertion into the transition metal hydride bond (TM–H bond) has attracted chemists' continued attention, and studies on the CO_2 insertion into the TM–H bond have served as a model to understand the role of hydrogen activated as hydride in the hydrogenation of CO_2 [9,10].

Hazari and co-workers showed that CO_2 reacted with ^{tBu2}(PCP)Ni–H (PCP = 2,6-bis((phosphaneyl)methyl)phenyl) within minutes at room temperature forming the ^{tBu2}(PCP)Ni-(O)-formate, which was characterized by X-ray crystallography (CSD entry: UMAPAA) [11]. The $^{13}CO_2$ labeling showed that the insertion of CO_2 into ^{tBu2}(PCP)Ni–H is reversible, and the barrier for insertion of CO_2 determined by the experimental Eyring

plot was 16.3 kcal mol^{-1} (Figure 1) [11,12]. The solvent effect on the reaction rate with an order of THF (6.8 ± 0.7 M^{-1} s^{-1}) < benzene (15 ± 2 M^{-1} s^{-1}) < acetone (51 ± 5 M^{-1} s^{-1}) < pyridine (130 ± 1 M^{-1} s^{-1}) < MeCN (220 ± 2 M^{-1} s^{-1}) was observed for the insertion of CO_2, and this order agrees with the order of the relative Lewis acidities of the above solvents [12].

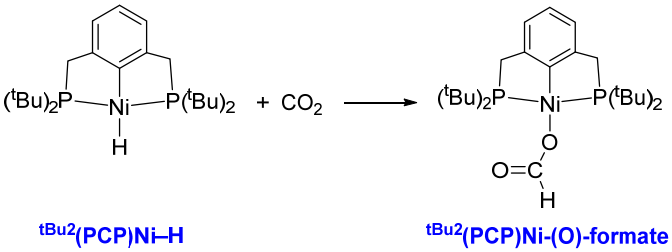

Figure 1. Reaction of CO_2 with ^{tBu2}(PCP)Ni-H.

Three major steps for the CO_2 insertion into Ni–H to form Ni-(O)-formate are proposed, including (1) the hydride transfer to the Ni-(H)-formate, (2) the rearrangement of the Ni-(H)-formate to form Ni-(O)-formate, and (3) the isomerization of the Ni-(O)-formate (Scheme 1) [12,13]. The stepwise pathway (1 → 2 → TS-2-3 → 3 → TS-3-4*i* → 4*i* → TS-4*i*-4 → 4, Scheme 1) and concerted pathway (1 → 2 → TS-3-4*i* → 4*i* →TS-4*i*-4 → 4, Scheme 1) have been proposed for the CO_2 insertion into transition metal hydride (TM–H) complexes. ^{tBu2}(PCP)Ni–H (PCP = 2,6-bis((phosphaneyl)methyl)phenyl) and its substituted analogs usually follow the stepwise pathway, and it is also true for the *cis*-Co(dmpe)$_2$H (dmpe = 1,2-bis(dimethylphosphaneyl)ethane) [14]. However, CO_2 insertion into the Ir–H complexes (Cp*(6,6′-dhbp)Ir–H)[OTf] and (Cp*(6,6′-dmbp)Ir–H)[OTf] (6,6′-dhbp = 6,6′-dihydroxybipyridine, 6,6′-dmbp = 6,6′-dimethoxybipyridine) [15], *cis*-Ru(dmpe)$_2$H$_2$ (dmpe = 1,2-bis(dimethylphosphaneyl)ethane) [16], and (CNN)(dppb)Ru–H (CNN = 2-aminomethyl-6-tolylpyridine, dppb = 1,4-bis-(diphenylphosphino)butane) [17] follows the concerted pathway without the observation of TM-(H)-formate. These different pathways raise the concern of whether the palladium analog, ^{tBu2}(PCP)Pd–H, and the cobalt analog, ^{tBu2}(PNP)Co–H (PNP = 2,6-bis((phosphaneyl)methyl)pyridyl), also follow the same stepwise pathway in the CO_2 insertion as ^{tBu2}(PCP)Ni–H. The four-centered transition state (**TS-3-4*i***) in Scheme 1) is suggested as the rate-determining transition state, and the rearrangement of the Ni-(H)-formate to form Ni-(O)-formate (3 → TS-3-4*i* → 4*i*, Scheme 1) is shown as the overall rate-determining step (RDS) [12,18]. However, the structure and its electronic characterization of Ni-(H)-formate are not fully determined, which needs further comprehensive investigations.

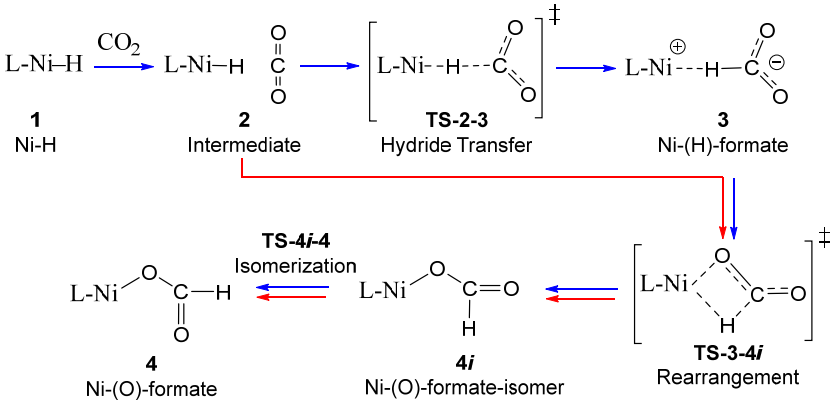

Scheme 1. Proposed pathway for the CO_2 insertion into nickel hydride complex.

In this contribution, to understand the role of hydrogen, activated as a hydride form, in the hydrogenation of CO_2, the detailed reaction mechanism of CO_2 insertion into nickel

hydride was investigated by density functional theory (DFT) computations. With the obtained rate-determining step (RDS), a series of square planar transition metal hydride (TM–H, TM = Ni, Pd, and Co) complexes (Figure 2) with various steric and electronic effects were studied for the insertion of CO_2 into the transition metal hydride (TM–H) bond. The activities of TM–H complexes in the reaction of CO_2 insertion were then parameterized, and the possible structure–activity relationship was also modeled, which light the way to the design of a more efficient Ni–H complex in the conversion of CO_2 to formate.

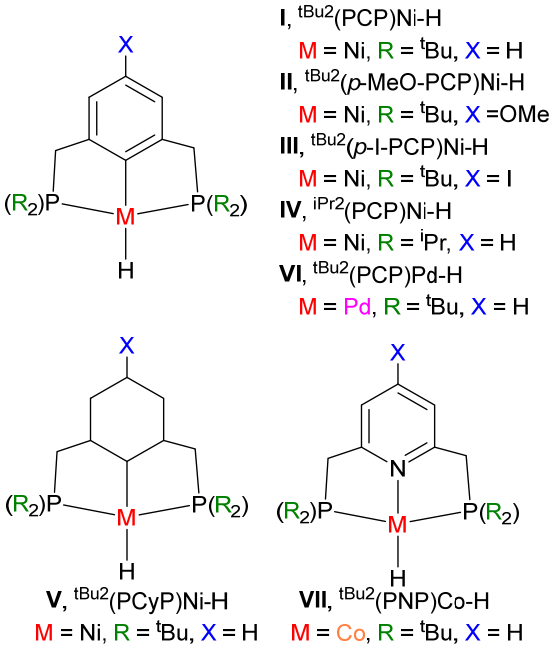

Figure 2. Studied transition metal hydride (TM–H) complexes **I** to **VII** for CO_2 insertion.

2. Computational Methods

Gas-phase geometry optimizations were carried out with B3LYP/BS1 [19–22] using Gaussian 16 (Revision C 01) [23]. In basis set 1 (BS1), the modified-LANL2DZ [24,25] basis set and LANL2DZ ECP were used for Ni, Co, and Pd; the LANL2DZ(*d*,*p*) [24,26] basis set and LANL2DZ ECP were used for P and I; the 6-31G(*d*′) [27–30] basis sets were used for all other atoms (C, O, N, and H). The self-consistent reaction field (SCRF) single-point computations in tetrahydrofuran (THF) were performed with the solvation model based on density (SMD) [31] and the Ahlrichs redefined Def2-TZVP [32,33] basis sets (H, C, O, N, P, I, Ni, Co, and Pd) with the energy-adjusted pseudopotential [33] for Pd (BS2). The hydricity (ΔG_{H^-}) of each metal hydride was calculated using the equation presented in Scheme S1 [34–36]. Grimme's D3 [37] dispersion with Becke–Johnson damping [D3(BJ)] [38] and the automatic density fitting approximation [39,40] with pure spherical harmonic 5*d* and 7*f* functions were utilized for all computations. All located minima were verified by vibrational frequency computations with no imaginary frequency, and all located transition states were obtained with only one imaginary frequency. The IRC (intrinsic reaction coordinate) computations from the located transition states were performed, and both directions of the reaction path following the transition state were computed [41]. The Gaussian 16 default ultrafine integration grid, 2-electron integral accuracy of 10^{-12}, and SCF convergence criterion of 10^{-8} were used for all computations. All computations were performed at 1 atm and 298.15 K. The electron density of the bond critical point [$r_{(BCP)}$] based on Bader's theory of atoms-in-molecules (AIMs) [42–44] and the natural adaptive orbital (NAdO) [45] were calculated by the Multiwfn package (version 3.8) [46,47] and were visualized by the VMD package (version 1.9.3) [48,49]. The SambVca (version 2.1) [50–52] web application was used to illuminate the steric hindrance of the ligand with parameters of percentages of buried volume (%V_{Bur}) [53] and the steric map (Table S4) [54]. Gibbs

free energies from SMD(THF)-B3LYP-D3(BJ)/BS2//B3LYP-D3(BJ)/BS1 computations are reported in the main text and are given in kcal mol^{-1}.

3. Results and Discussion

The DFT-optimized structures of nickel hydride (Ni–H) complex ^{tBu2}(PCP)Ni–H (PCP = 2,6-bis((phosphaneyl)methyl)phenyl) and its [Ni^{II}]-(O)-formate were matched with the reported X-ray crystal structures (CSD entries: SURZIP and UMAPAA). Relatively small root-mean-square deviations (RMSDs, in Å) of 0.1680 and 0.1240 were obtained (Table S1), which demonstrated the good reliability and accuracy of the optimization methodology [55]. For comparison, the optimizations of ^{tBu2}(PCP)Ni–H and its [Ni^{II}]-(O)-formate complex were also performed with SMD(THF)-B3LYP-D3(BJ)/BS2, and the RMSD values (in Å) for SMD(THF)-B3LYP-D3(BJ)/BS2 optimized structures were 0.092 and 0.0886, respectively (Table S1). The relatively small differences in the RMSD values between the B3LYP-D3(BJ)/BS1 optimization and the SMD(THF)-B3LYP-D3(BJ)/BS2 optimization demonstrate the good reliability and accuracy of B3LYP-D3(BJ)/BS1 [56–58].

To investigate the CO_2 insertion into nickel hydride complexes, the following three sections are discussed, including the (1) mechanism of CO_2 insertion into the Ni–H bond of ^{tBu2}(PCP)Ni–H; (2) analysis of Ni-(H)-formate intermediate **3**, and (3) parameterized activity and modeling of Ni–H complexes for CO_2 insertion.

3.1. Mechanism of CO_2 Insertion into Ni–H Bond of ^{tBu2}(PCP)Ni–H

As presented in Scheme 1, three major steps including (1) the hydride transfer to form the Ni-(H)-formate **3** (**1** → **3**, Figure 3), (2) rearrangement of the Ni-(H)-formate to form Ni-(O)-formate (**3** → ***4i***, Figure 3), and (3) isomerization of the Ni-(O)-formate (***4i*** → **4**, *exo*→*endo*, Figure 3) are investigated for the CO_2 insertion reaction. First, a direct hydride transfer from the ^{tBu2}(PCP)Ni–H structure **1** to the CO_2 (Ni–H ··· CO_2 adduct **2**) generates the Ni-(H)-formate intermediate **3** (9.6 kcal mol^{-1}, Figure 3) with a Gibbs free energy of activation ($\Delta G^{\ddagger}$) of 10.6 kcal mol^{-1}. The Ni ··· H atom distance in Ni-(H)-formate intermediate **3** is 1.610 Å, which is longer than that in Ni–H complex **1** (1.551 Å). A linear Ni-H-$C_{(CO2)}$ bond angle (197.97°) in Ni-(H)-formate intermediate **3** is observed, which shows the existence of electrostatic attraction between the Ni center and the H atom in **3** Ni-(H)-formate (see further discussions below on intermediate **3**). It is also noted that the formation of the Ni-(H)-formate intermediate **3** from the Ni–H ··· CO_2 adduct **2** is endergonic, and the relative Gibbs free energies for **3** Ni-(H)-formate and **2** Ni–H ··· CO_2 adduct are 9.6 and 4.3 kcal mol^{-1}, respectively. The possible direct proton transfer from the Ni–H to the CO_2 in Ni–H ··· CO_2 adduct **2** is also modeled (1 → 2 → TS-2-5 → 5, Figure S2), and a Ni-(O)-hydroxy(oxo)methanide intermediate **5** with a Gibbs free energy of 36.7 kcal mol^{-1} is located. This direct proton transfer has a Gibbs free energy of activation of 57.3 kcal mol^{-1} (TS-2-5, Figure S2), which is significantly unfavorable compared to the direct hydride transfer in Ni–H ··· CO_2 adduct **2** to form Ni-(H)-formate **3** (10.6 kcal mol^{-1}, Figure 3) and is excluded for the pathway of CO_2 insertion into nickel hydride [36]. Another unfavorable CO pathway is also explored (1 → 2 → 3*i* → TS-3*i*-6 → 6→ 7, Figure S3). The proposed CO pathway starts with a Ni-(H)-formate isomer ***3i***, which has a nonlinear Ni-H-C bond angle of 160.30° instead of the linear Ni-H-C bond angle of 179.97° in Ni-(H)-formate **3**. The following transition state TS-3*i*-6 from ***3i*** forms the Ni-carboxylic acid intermediate **6** with a Gibbs free energy of activation of 49.8 kcal mol^{-1}, which is the overall rate-determining step (RDS) in the proposed CO pathway. The final Ni-carbonyl intermediate **7** was generated via the dissociation of the hydroxyl group from the Ni-carboxylic acid intermediate **6**, and a relatively high Gibbs free energy of 32.3 kcal mol^{-1} for intermediate 7 was obtained. The significantly high Gibbs free energy of activation of 49.8 kcal mol^{-1} from the located RDS (TS-3*i*-6, Figure S3) limits the possibility of the CO pathway.

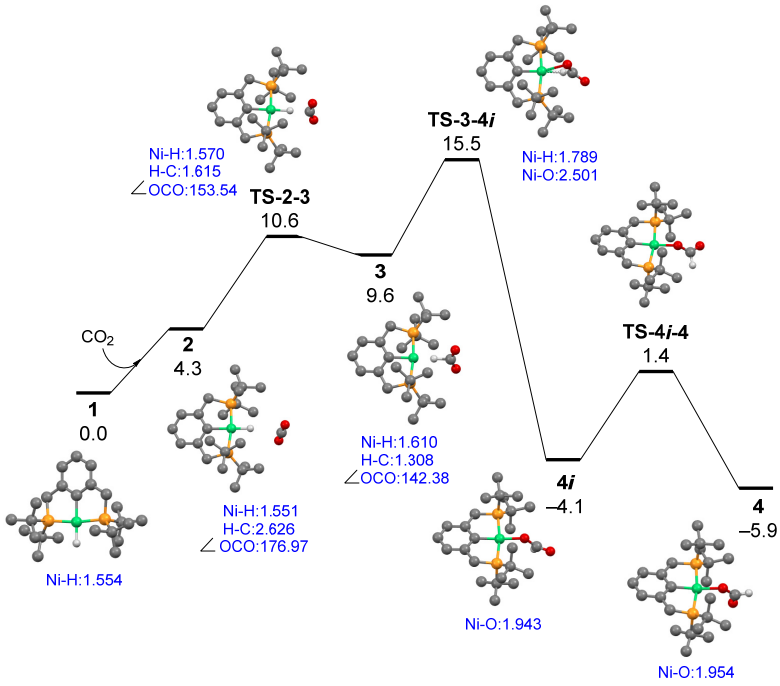

Figure 3. Free energy diagram for CO_2 insertion into **I**, ^{tBu2}(PCP)Ni–H. Selected atom distances are given in Å, selected bond angles are given in degrees, and $\Delta G^\circ/\Delta G^\ddagger$ are in kcal mol^{-1}. Hydrogen atoms except the hydride are omitted for clarity. Color code: green, Ni; yellow, P; gray, C; red, O; white, H.

Once the Ni-(H)-formate intermediate **3** is formed, the following rearrangement caused by the nucleophilic attraction of one terminal O atom on the Ni center forms the Ni-(O)-(*exo*)formate **4*i*** (3→4*i*, Figure 3) with a Gibbs free energy of activation of 15.5 kcal mol^{-1}. A bent Ni-O-C bond angle (131.23°) is shown in Ni-(O)-(*exo*)formate **4*i*** with an *exo* formate fragment. The formation of **4*i*** Ni-(O)-(*exo*)formate is exergonic, and the relative Gibbs free energy for **4*i*** Ni-(O)-(*exo*)formate is –4.1 kcal mol^{-1}. The isomerization of **4*i*** Ni-(O)-(*exo*)formate forms the final product **4** Ni-(O)-(*endo*)formate (4*i*→4, *exo*→*endo*, Figure 3) with a Gibbs free energy of activation ($\Delta G^\ddagger$) of 1.4 kcal mol^{-1}. The DFT-optimized structure of final product **4** Ni-(O)-(*endo*)formate matches well with its reported X-ray crystal structures (CSD entry: UMAPAA) with an RMSD value (in Å) of 0.1240 (Table S1). The overall stepwise pathway for the capture of CO_2 by ^{tBu2}(PCP)Ni–H **1** to form **4** Ni-(O)-(*endo*)formate (1 → 4, Figure 3) is favorable at –5.9 kcal mol^{-1} from the computations of SMD(THF)-B3LYP-D3(BJ)/BS2//B3LYP-D3(BJ)/BS1, which is consistent with the SMD(THF)-B3LYP-D3(BJ)/BS2 computed value of –5.2 kcal mol^{-1}. The computed Gibbs barrier for the overall rate-determining step (RDS) based on the energetic span/transition state theory is determined as 15.5 kcal mol^{-1} (**TS-3-4*i***, Figure 3), which agrees with the experimental value of 16.3 kcal mol^{-1} determined by the Eyring plot [12].

With the established pathway of CO_2 insertion into ^{tBu2}(PCP)Ni–H (PCP = 2,6-bis((phosphaneyl)methyl)phenyl) (Figure 3), the catalytic activities of a series of square planar transition metal hydride complexes (**I** to **VII**, Figure 2) for CO_2 insertion are investigated. The parent ^{tBu2}(PCP)Ni–H complex (**I**) is modified by the introduced electron-donating (*p*-OMe, ^{tBu2}(*p*-MeO-PCP)Ni–H, **II**) and electron-withdrawing groups (*p*-iodo, ^{tBu2}(*p*-I-PCP)Ni–H, **III**) on the *para* position of the phenyl fragment. To evaluate the steric effect in the CO_2 insertion, two tert-butyl groups (^{t}Bu$_2$) in ^{tBu2}(PCP)Ni–H complex (**I**) are replaced by two isopropyl groups (^{i}Pr$_2$), forming ^{iPr2}(PCP)Ni–H (**IV**). To address the electronic effect, the phenyl group in ^{tBu2}(PCP)Ni–H complex (**I**) is changed to a cyclohexyl group (Cy), forming ^{tBu2}(PCyP)Ni–H (**V**) (PCyP = 2,6-bis((phosphaneyl)methyl)cyclohexyl). To further confirm the established stepwise pathway (1 → 2 → TS-2-3 → 3 → TS-3-4*i* → 4*i* → TS-4*i*-4 → 4, Scheme 1 and Figure 3) of CO_2 insertion into TM–H complexes, the structural analogs

^{tBu2}(PCP)Pd–H (**VI**) and ^{tBu2}(PNP)Co–H (**VII**) (PNP = 2,6-bis((phosphaneyl)methyl)pyridyl) are also computationally modeled for the CO_2 insertion into the Pd–H bond and Co–H bond, respectively.

The computed hydricities and Gibbs free energies of activation for these seven square planar transition metal hydride complexes (TM–H, TM = Ni, Pd, and Co) (**I** to **VII**, Figure 2) for CO_2 insertion are summarized in Table 1. The APT charge of the transition metal atom in the axially vacant $[TM]^+$ and the percentages of buried volume in the axially vacant $[TM]^+$ are also included in Table 1. The Gibbs free energies of other intermediates on the computed pathway are presented in Figure S4. It is worth noting that the TM-(H)-formate intermediate for the CO_2 insertion into all seven square planar transition metal hydride (TM–H) complexes (**I** to **VII**) were located. As one major difference between the stepwise pathway and concerted pathway in the CO_2 insertion, the TM-(H)-formate intermediate could only be observed in the stepwise pathway, as pointed out by Hazari and co-workers [12,59]. In this study, the TM-(H)-formate intermediates for all seven square planar transition metal hydride (TM–H, TM = Ni, Pd, and Co) complexes were successfully located, and no direct conversion from the TM–H $\cdots$ CO_2 adduct and TM-(O)-formate could be established. This suggests that no reasonable concerted pathway in the CO_2 insertion for the seven square planar TM–H complexes (TM = Ni, Pd, and Co) could be obtained. Compared to the linear Ni-H-C bond angle (179.97°) in Ni-(H)-formate intermediate **3** of Ni–H complex **I**, the nonlinear Pd-H-C bond angle (152.45°) in the Pd-(H)-formate intermediate of Pd–H complex **VI** and the nonlinear Co-H-C bond angle (133.27°) in the Co-(H)-formate intermediate of Co–H complex **VII** were observed, which affected the electron densities of TM $\cdots$ H bond critical points and $C_{(formate)}$-H bond critical points, leading to various Gibbs barriers for the RDS (Table 1), but did not change the stepwise pathway. The geometrical commonality of the square planar structure could be used to explain the comparable stepwise pathway for the CO_2 insertion into all seven TM–H complexes (TM = Ni, Pd, and Co).

Table 1. Computed hydricity, $\%V_{Bur}$, and $\Delta G^{\ddagger}$ for TM–H complexes **I** to **VII**.

Species	Hydricity	TS-2-3	TS-3-4*i*	APT	$\%V_{Bur}$	*k* (M^{-1} s^{-1})
I, ^{tBu2}(PCP)Ni–H	50.6	10.6	15.5	0.132	81.4	6.8 ± 0.7
II, ^{tBu2}(*p*-MeO-PCP)Ni–H	50.1	10.7	15.3	0.139	81.4	11.7 ± 1
III, ^{tBu2}(*p*-I-PCP)Ni–H	52.3	11.1	15.9	0.139	81.4	1.6 ± 0.2
IV, ^{iPr2}(PCP)Ni–H	53.2	11.5	14.7	0.108	77.4	4400
V, ^{tBu2}(PCyP)Ni–H	43.3	10.4	10.8	0.047	83.4	-
VI, ^{tBu2}(PCP)Pd–H	48.7	10.5	15.1	0.052	81.3	-
VII, ^{tBu2}(PNP)Co–H	41.2	8.4	8.9	−0.116	77.7	-

Note: APT is the APT charge of transition metal atom in the axially vacant $[TM]^+$, $\%V_{Bur}$ is the percentage of buried volume in the axially vacant $[TM]^+$. Reaction rate (*k*) is experimentally determined at 298 K in THF.

Comparisons of the computed $\Delta G^{\ddagger}$ of the RDS (**TS-3-4*i***) of ^{tBu2}(PCP)Ni–H (**I**), ^{tBu2}(*p*-MeO-PCP)Ni–H (**II**), and ^{tBu2}(*p*-I-PCP)Ni–H (**III**) show that the introduced electron-withdrawing group (*p*-iodo) decreases the catalytic activity with the highest $\Delta G^{\ddagger}$ of 15.9 kcal mol^{-1} and the introduced electron-donating group (*p*-OMe) increases the catalytic activity with the lowest $\Delta G^{\ddagger}$ of 15.3 kcal mol^{-1}. This computed order of $\Delta G^{\ddagger}$ of the RDS (**III** > **I** > **II**) is consistent with the experimentally determined reaction rate (*k*) (1.6 ± 0.2 for **III**, 6.8 ± 0.7 for **I**, and 11.7 ± 1 M^{-1} s^{-1} for **II**). The computed hydricities of ^{tBu2}(*p*-I-PCP)Ni–H (**III**), ^{tBu2}(PCP)Ni–H (**I**), and ^{tBu2}(*p*-MeO-PCP)Ni–H (**II**) are 52.3, 50.6, and 50.1 kcal mol^{-1}, respectively, and an order for Ni–H bond strength of **III** > **I** > **II** is concluded. The RDS (**TS-3-4*i***) is the nucleophilic attraction of the terminal O atom on the Ni center in **3** Ni-(H)-formate, forming the **4*i*** Ni-(O)-(*exo*)formate, and the effect of the APT charge of the transition metal atom in the axially vacant $[TM]^+$ and the effect of the percentages of buried volume in the axially vacant $[TM]^+$ on the CO_2 insertion into all seven TM–H complexes are also evaluated. Identical values of $\%V_{Bur}$ in the axially vacant $[TM]^+$ complexes **I**,

II, and **III** are obtained (81.4, Table 1), which suggest that the introduced *para* group has a negligible effect on the rigid PCP structure and on the geometry of the two tert-butyl groups ($^{t}Bu_2$). However, the $\%V_{Bur}$ decreases from 81.4 to 77.4 for ^{iPr2}(PCP)Ni–H (**IV**) when the two tert-butyl groups ($^{t}Bu_2$) in ^{tBu2}(PCP)Ni–H complex (**I**) are replaced by two isopropyl groups ($^{i}Pr_2$). The computed $\Delta G^{‡}$ of the RDS (**TS-3-4*i***) for ^{iPr2}(PCP)Ni–H (**IV**) is 14.7 kcal mol^{-1}, which is also lower than those for ^{tBu2}(*p*-I-PCP)Ni–H (**III**), ^{tBu2}(PCP)Ni–H (**I**), and ^{tBu2}(*p*-MeO-PCP)Ni–H (**II**), leading to a faster reaction rate (*k*) of 4400 M^{-1} s^{-1}. Computational results show that ^{tBu2}(PCyP)Ni–H (**V**) has the lowest $\Delta G^{‡}$ of the RDS among all the five Ni–H species (**I** to **V**) for the CO_2 insertion (10.8 kcal mol^{-1}) and the lowest hydricity (43.3) among all the five Ni–H species, but the highest buried volume in the axially vacant $[Ni]^{+}$ (83.4). This inconsistent observation suggests that the steric effect of CO_2 is less important than the electronic effect of the Ni–H complexes in the CO_2 insertion. Compared to ^{Bu2}(PCP)Ni–H complex (**I**), the structural analog ^{tBu2}(PCP)Pd–H (**VI**) presents a similar stepwise pathway for the CO_2 insertion with a Pd-(H)-formate intermediate, and a slightly lower $\Delta G^{‡}$ of the RDS (15.1 kcal mol^{-1}) for ^{tBu2}(PCP)Pd–H (**VI**) is obtained. It is an interesting finding that the cobalt analog, ^{tBu2}(PNP)Co–H (**VII**) (PNP = 2,6-bis((phosphaneyl)methyl)pyridyl), shows the lowest $\Delta G^{‡}$ of the RDS (8.9 kcal mol^{-1}) among all seven square planar TM–H complexes (**I** to **VII**), presents the lowest hydricity of 41.2 kcal mol^{-1}, and also has the smallest buried volume in the axially vacant $[Co]^{+}$ (77.7) among all six tert-butyl substituent ($^{t}Bu_2$) hydride complexes (**I** to **III** and **V** to **VII**). Compared to the anionic phenyl group and Ni(II) atom in ^{tBu2}(PCP)Ni–H complex (**I**), the neutral pyridyl group and the Co(I) atom in ^{tBu2}(PNP)Co–H (**VII**) produce an electron-rich Co center, leading to a weaker Co–H bond and a lower value of $\Delta G^{‡}$ for the RDS.

*3.2. Analysis of Ni-(H)-Formate Intermidiate **3***

To further illustrate the electrostatic attraction between the Ni center and the H atom in **3** Ni-(H)-formate, atoms-in-molecules (AIMs) analysis and the natural adaptive orbital (NadO) of Ni-(H)-formate complexes are performed (Figures 4 and 5, Tables S2 and S3). A nonnegligible electron density of a Ni $\cdots$ H bond critical point [$r_{(BCP)}$] from AIM analysis is observed, and the $r_{(BCP)}$ for the Ni $\cdots$ H bond in the Ni-(H)-formate complexes **I**, **II**, and **III** are 0.0786, 0.0782, and 0.0801, respectively (Figure 4). For comparisons, the $r_{(BCP)}$ for the $C_{(formate)}$-H bond in Ni-(H)-formate complexes **I**, **II**, and **III** are 0.1527, 0.1549, and 0.1473, respectively. The order of the relative strength of the Ni $\cdots$ H interaction in Ni-(H)-formate is **III** > **I** > **II**, which is consistent with the value of positive charge of the Ni atom in complexes **III**, **I**, and **II** introduced by the electron-withdrawing group (*p*-iodo) and electron-donating group (*p*-OMe). The $r_{(BCP)}$ for Ni $\cdots$ H interaction in Ni-(H)-formate complexes **IV** and **V** are 0.0800 and 0.0730, respectively, and the $r_{(BCP)}$ for the $C_{(formate)}$-H bond in Ni-(H)-formate complexes **IV** and **V** are 0.1464 and 0.1673, respectively (Table S2). The Ni-(H)-formate complex **V** with the nonplanar and nonaromatic cyclohexyl ligand presents the smallest $r_{(BCP)}$ for the Ni $\cdots$ H bond (0.0730) and the biggest $r_{(BCP)}$ for the $C_{(formate)}$-H bond (0.1673) in Ni-(H)-formate among all five Ni complexes. As the electron delocalization in Ni-(H)-formate complex **V** is limited by the nonplanar and nonaromatic cyclohexyl ligand compared to the aromatic phenyl and substituted phenyl groups in Ni-(H)-formate complexes **I**, **II**, **III**, and **IV**, the weakest Ni $\cdots$ H interaction in Ni-(H)-formate complex **V** is expected and also verified. Compared to the electron density of Ni $\cdots$ H in Ni-(H)-formate complexes **I**, **II**, and **III** (0.0786, 0.0782, and 0.0801, respectively), the electron density of the Co $\cdots$ H bond critical point [$r_{(BCP)}$] is quite small for VII (0.0698, Figure 4), which shows that the Co $\cdots$ H bond interaction is much weaker than the Ni $\cdots$ H ones. Not surprisingly, the strongest $C_{(formate)}$-H bond with an $r_{(BCP)}$ of 0.1838 for Co-(H)-formate (VII) among all the TM-(H)-formate intermediates was observed. As the overall rate-determining step (RDS) is the nucleophilic attraction of the terminal O atom on the TM center in TM-(H)-formate to form TM-(O)-(exo)formate (TS-3-4*i*), a lower Gibbs barrier for this conversion induced by the weaker TM $\cdots$ H bond is anticipated. The cobalt pyridine

intermediate Co-(H)-formate (VII) with the weakest TM ··· H bond has the lowest Gibbs barrier for the RDS among all the TM–H complexes (8.9 kcal mol^{-1}, Table 1).

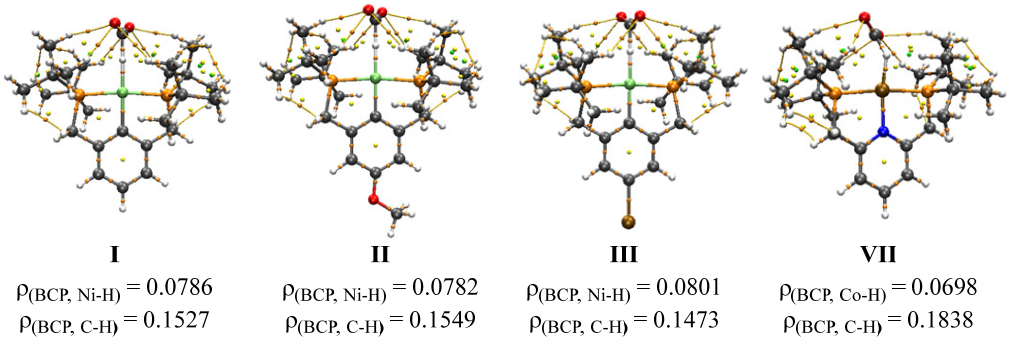

Figure 4. The critical points from atoms-in-molecules (AIMs) analysis of TM-(H)-formate complexes **I**, **II**, **III**, and **VII**. The orange balls represent the BCP (bond critical point), the yellow balls represent the ring critical point (RCP), and the bond paths for hydrogen bonds are shown in orange.

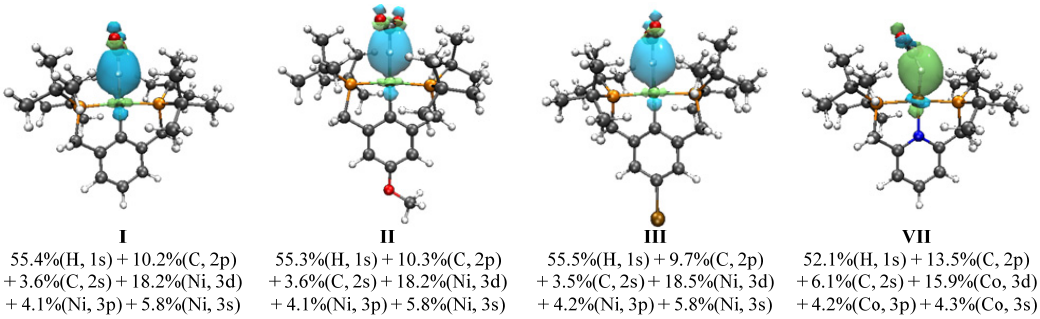

Figure 5. The natural adaptive orbitals (NAdOs) with their eigenvalues for the TM-H-C interaction in the TM-(H)-formate complexes **I**, **II**, **III**, and **VII**. Only the first NAdOs with the isovalue of 0.05 are presented in the main text.

The Ni-H-C interaction in the Ni-(H)-formate complexes is also investigated by the natural adaptive orbitals (NAdOs), and comparable NAdO compositions in complexes **I**, **II**, and **III** are obtained (Figure 5). A slightly higher contribution of the 3*d* orbital from the Ni atom for the NAdO in Ni-(H)-formate complex **III** (18.5%) compared to those in Ni-(H)-formate complexes **I** (18.2%) and **II** (18.2%) is observed, which is caused by the introduced electron-withdrawing group (*p*-iodo), demonstrating the stronger Ni ··· H interaction in Ni-(H)-formate complex **III**. Compared to the NAdO orbital contributions in the Ni-(H)-formate complexes **I**, **II**, and **III**, a noticeably higher contribution from the 2*p* orbital of the C atom (13.5%) and a lower contribution from the 3*d* orbital of the Co atom (15.9%) for the Co-H-C NAdO in the Co-(H)-formate complex **VII** were observed. The non-linear Co-H-C bond angle (133.27°) in Co-(H)-formate complex **VII** compared to the linear Ni-H-C bond angle (179.97°) in Ni-(H)-formate complex **I** may cause the different NAdO orbital contributions.

3.3. Parameterized Activity and Modeling of Ni–H Complexes for CO_2 Insertion

The nucleophilic attraction of the terminal O atom on the Ni center in **3** Ni-(H)-formate to form **4*i*** Ni-(O)-(*exo*)formate (3 → TS-3-4*i* → 4*i*, Figure 3 and Table 1) is demonstrated as the overall RDS for CO_2 insertion into nickel hydride, and the effect of the APT charge of the Ni atom in the axially vacant $[Ni]^+$ complexes on CO_2 insertion is confirmed. An excellent linear fitting (R^2 = 0.967) between the $\Delta G^‡$ of the RDS for Ni–H complexes **I** to **V** and the APT charges of Ni atoms in the related axially vacant $[Ni]^+$ complexes is observed (Figure 6). An acceptable linear fitting (R^2 = 0.8002) between the $\Delta G^‡$ of the RDS for all

seven transition metal hydride complexes (**I** to **VII**) and the APT charges of transition metals in the related axially vacant $[TM]^+$ complexes is also obtained (Figure S6).

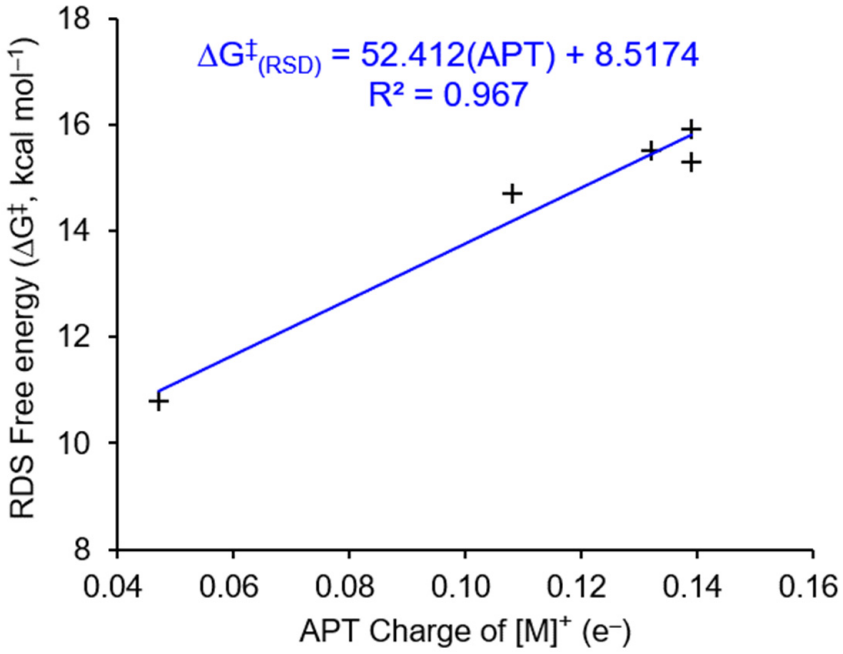

Figure 6. The linear fitting between the $\Delta G^‡$ of RDS for Ni–H complexes **I** to **V** and the APT charges of Ni atoms in the related $[Ni]^+$.

In an attempt to achieve a structure–activity relationship in the capture of CO_2 by transition metal hydride complexes (TM–H), the correlation between the $\Delta G^‡$ of the RDS for Ni–H complexes **I** to **V** and the computed hydricities is fitted (Figure 7). An appropriate linear fitting (R^2 = 0.8164) between the $\Delta G^‡$ of the RDS for Ni–H complexes **I** to **V** and the computed hydricities is achieved, but the second-order polynomial fitting provides a better accuracy (R^2 = 0.973) (Figure 7). An improved second-order polynomial fitting between the $\Delta G^‡$ of the RDS and the computed hydricities for all seven TM–H complexes (**I** to **VII**) is also observed (R^2 = 0.9832) (Figure S7). The above discussed second-order polynomial fittings suggest the existence of the optimal value of hydricity for the reaction of CO_2 insertion and also indicate that a single-parameter model is not adequate to present a convincing structure–activity relationship in the capture of CO_2 by TM–H complexes. With the obtained RDS for CO_2 insertion into nickel hydride (3 → TS-3-4*i* → 4*i*, Figure 3 and Table 1), the multi-parameter models (Scheme 2) including the APT charge of Ni atoms in the axially vacant $[Ni]^+$ complexes, the buried volume ($\%V_{Bur}$) in the axially vacant $[Ni]^+$ complexes, and the computed hydricities of Ni–H complexes are investigated. An excellent two-parameter model (R^2 = 0.9872, Equation (1), Scheme 2) and a three-parameter model (R^2 = 0.9967, Equation (2), Scheme 2) to quantitatively describe the overall $\Delta G^‡$ of the RDS for CO_2 insertion into nickel hydride are established, which also demonstrate the dominant factor of the APT charge of Ni atoms in the axially vacant $[Ni]^+$ complexes for the reaction of CO_2 insertion, as illustrated in Figure 6.

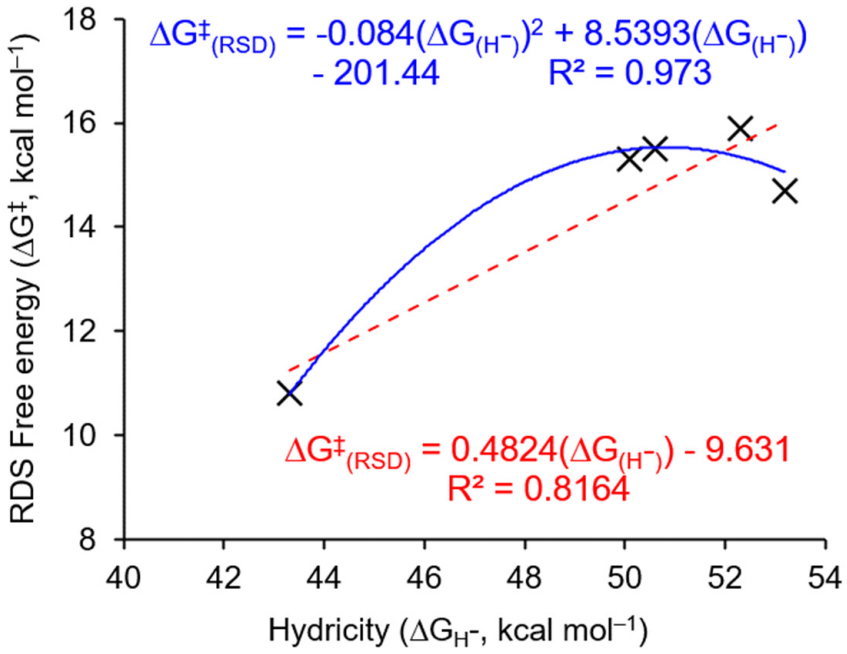

Figure 7. The fitting between the $\Delta G^{\ddagger}$ of RDS for Ni–H complexes **I** to **V** and the computed hydricities. The blue line represents the second-order polynomial fitting and the red line represents the linear fitting.

$$\Delta G^{\ddagger}_{RDS} = APT(49.78) + \%V(Bur)(-0.14) + 20.39 \qquad R^2 = 0.9872 \qquad Eq\ 1$$

$$\Delta G^{\ddagger}_{RDS} = APT(33.23) + \%V(Bur)(0.12) + \Delta G(H^-) - 11.90 \quad R^2 = 0.9967 \qquad Eq\ 2$$

Scheme 2. The multi-parameter models for the $\Delta G^{\ddagger}$ of RDS for Ni–H complexes **I** to **V**. In Equations (1) and (2), APT is the APT charge of Ni atom in the axially vacant $[Ni]^+$; $\%V_{Bur}$ is the percentages of buried volume in the axially vacant $[Ni]^+$.

4. Conclusions

To convert CO_2 into the useful chemical feedstock and to achieve the target of carbon neutrality, the capture and utilization of CO_2 by transition metal hydride complexes (TM–H) via the homogeneous hydrogenation of CO_2 are desired. Theoretical insights into the hydrogenation of CO_2 have been benefited from the computational modeling. The activation of an H_2 molecule to form the hydride species, the following CO_2 insertion into the TM–H bond, and the release of formate are the key steps in the hydrogenation of CO_2 to generate formate. The computational investigations for the homogeneous CO_2 insertion into ^{tBu2}(PCP)Ni–H (PCP = 2,6-bis((phosphaneyl)methyl)phenyl) are performed in this study. The reaction of CO_2 insertion into Ni–H is followed by a stepwise pathway, and the rearrangement of the Ni-(H)-formate to form Ni-(O)-formate is the overall rate-determining step (RDS, $\Delta G^{\ddagger}$ = 15.5 kcal mol^{-1} for ^{tBu2}(PCP)Ni–H). The complexes with improved hydride donor abilities have promote the activities of CO_2 insertion with lower $\Delta G^{\ddagger}$ (15.5 kcal mol^{-1} for ^{tBu2}(PCP)Ni–H, 15.3 kcal mol^{-1} for ^{tBu2}(*p*-MeO-PCP)Ni–H, and 10.8 kcal mol^{-1} for ^{tBu2}(PCyP)Ni–H). The structure–activity relationship of homogeneous CO_2 insertion with a series of square planar transition metal hydride complexes (TM–H) is evaluated. The single-parameter and multi-parameter models show that the charge of the Ni atom in the axially vacant $[Ni]^+$ complexes is the dominant factor on CO_2 insertion with an excellent linear fitting (R^2 = 0.967). The parameterized activities and modeled structure–activity relationship provided here are the helpful references to the design of a more efficient Ni–H complex in the homogeneous hydrogenation of CO_2 to formate.

Supplementary Materials: The following supporting information can be downloaded at: https://www.mdpi.com/article/10.3390/catal12070790/s1, Table S1: The matched structures; Table S2: The AIM analysis; Table S3: The first three NAdOs; Table S4: The steric map of optimized TM–H; Table S5: DFT-computed energies for species; Table S6: Cartesian coordinates; Scheme S1: Equation used to calculate the hydricity; Scheme S2: The multi-parameter models; Figure S1: Free energy diagram for CO_2 insertion into ^{tBu2}(PCP)Ni–H; Figure S2: Free energy diagram for proton transfer; Figure S3: Free energy diagram for formate pathway and CO pathway; Figure S4: Free energy diagram for CO_2 insertion into TM–H; Figure S5: The representations of 3D and 2D steric maps; Figures S6 and S7: The linear fitting; Figures S8–S11: IRC plots.

Author Contributions: M.Z.: conceptualization, investigation, formal analysis, writing—original draft; X.L.: investigation, formal analysis; Y.W.: visualization, formal analysis; H.Y.: data curation, formal analysis; G.L.: conceptualization, formal analysis, methodology, writing—review and editing, funding acquisition. All authors have read and agreed to the published version of the manuscript.

Funding: This research was supported by start-up funds from Xidian University (1018/10251210050).

Institutional Review Board Statement: Not applicable.

Informed Consent Statement: Not applicable.

Data Availability Statement: Not applicable.

Acknowledgments: We are grateful for the financial support from Xi'an International University and the start-up funds from Xidian University (1018/10251210050), and we thank the high-performance computing platform of Xidian University (XDHCPP) for computing support.

Conflicts of Interest: The authors declare no conflict of interest.

References

1. Hasan, M.M.F.; Rossi, L.M.; Debecker, D.P.; Leonard, K.C.; Li, Z.; Makhubela, B.C.E.; Zhao, C.; Kleij, A. Can CO_2 and Renewable Carbon Be Primary Resources for Sustainable Fuels and Chemicals? *ACS Sustain. Chem. Eng.* **2021**, *9*, 12427–12430. [CrossRef]
2. Saravanan, A.; Kumar, P.S.; Vo, D.-V.N.; Jeevanantham, S.; Bhuvaneswari, V.; Narayanan, V.A.; Yaashikaa, P.R.; Swetha, S.; Reshma, B. A comprehensive review on different approaches for CO_2 utilization and conversion pathways. *Chem. Eng. Sci.* **2021**, *236*, 116515. [CrossRef]
3. Valluri, S.; Claremboux, V.; Kawatra, S. Opportunities and challenges in CO_2 utilization. *J. Environ. Sci.* **2022**, *113*, 322–344. [CrossRef]
4. Kinzel, N.W.; Werlé, C.; Leitner, W. Transition Metal Complexes as Catalysts for the Electroconversion of CO_2: An Organometallic Perspective. *Angew. Chem. Int. Ed.* **2021**, *60*, 11628–11686. [CrossRef]
5. Navarro-Jaén, S.; Virginie, M.; Bonin, J.; Robert, M.; Wojcieszak, R.; Khodakov, A.Y. Highlights and challenges in the selective reduction of carbon dioxide to methanol. *Nat. Rev. Chem.* **2021**, *5*, 564–579. [CrossRef]
6. Zhang, S.; Fan, Q.; Xia, R.; Meyer, T.J. CO_2 Reduction: From Homogeneous to Heterogeneous Electrocatalysis. *Acc. Chem. Res.* **2020**, *53*, 255–264. [CrossRef]
7. Kostera, S.; Peruzzini, M.; Gonsalvi, L. Recent Advances in Metal Catalyst Design for CO_2 Hydroboration to C1 Derivatives. *Catalysts* **2021**, *11*, 58. [CrossRef]
8. Bai, S.-T.; De Smet, G.; Liao, Y.; Sun, R.; Zhou, C.; Beller, M.; Maes, B.U.W.; Sels, B.F. Homogeneous and heterogeneous catalysts for hydrogenation of CO_2 to methanol under mild conditions. *Chem. Soc. Rev.* **2021**, *50*, 4259–4298. [CrossRef] [PubMed]
9. Wang, W.-H.; Himeda, Y.; Muckerman, J.T.; Manbeck, G.F.; Fujita, E. CO_2 Hydrogenation to Formate and Methanol as an Alternative to Photo- and Electrochemical CO_2 Reduction. *Chem. Rev.* **2015**, *115*, 12936–12973. [CrossRef]
10. Jessop, P.G.; Joó, F.; Tai, C.-C. Recent advances in the homogeneous hydrogenation of carbon dioxide. *Coord. Chem. Rev.* **2004**, *248*, 2425–2442. [CrossRef]
11. Schmeier, T.J.; Hazari, N.; Incarvito, C.D.; Raskatov, J.A. Exploring the reactions of CO_2 with PCP supported nickel complexes. *Chem. Commun.* **2011**, *47*, 1824–1826. [CrossRef] [PubMed]
12. Heimann, J.E.; Bernskoetter, W.H.; Hazari, N.; Mayer, J.M. Acceleration of CO_2 insertion into metal hydrides: Ligand, Lewis acid, and solvent effects on reaction kinetics. *Chem. Sci.* **2018**, *9*, 6629–6638. [CrossRef] [PubMed]
13. Heimann, J.E.; Bernskoetter, W.H.; Hazari, N. Understanding the Individual and Combined Effects of Solvent and Lewis Acid on CO_2 Insertion into a Metal Hydride. *J. Am. Chem. Soc.* **2019**, *141*, 10520–10529. [CrossRef] [PubMed]
14. Kumar, N.; Camaioni, D.M.; Dupuis, M.; Raugei, S.; Appel, A.M. Mechanistic insights into hydride transfer for catalytic hydrogenation of CO_2 with cobalt complexes. *Dalton Trans.* **2014**, *43*, 11803–11806. [CrossRef]
15. Siek, S.; Burks, D.B.; Gerlach, D.L.; Liang, G.; Tesh, J.M.; Thompson, C.R.; Qu, F.; Shankwitz, J.E.; Vasquez, R.M.; Chambers, N.; et al. Iridium and Ruthenium Complexes of N-Heterocyclic Carbene- and Pyridinol-Derived Chelates as Catalysts for Aqueous

Carbon Dioxide Hydrogenation and Formic Acid Dehydrogenation: The Role of the Alkali Metal. *Organometallics* **2017**, *36*, 1091–1106. [CrossRef]
16. Whittlesey, M.K.; Perutz, R.N.; Moore, M.H. Facile insertion of CO_2 into the Ru-H bonds of $Ru(dmpe)_2H2$ (dmpe = $Me_2PCH_2CH_2PMe_2$): Identification of three ruthenium formate complexes. *Organometallics* **1996**, *15*, 5166–5169. [CrossRef]
17. Ramakrishnan, S.; Waldie, K.M.; Warnke, I.; De Crisci, A.G.; Batista, V.S.; Waymouth, R.M.; Chidsey, C.E.D. Experimental and Theoretical Study of CO_2 Insertion into Ruthenium Hydride Complexes. *Inorg. Chem.* **2016**, *55*, 1623–1632. [CrossRef]
18. Suh, H.-W.; Schmeier, T.J.; Hazari, N.; Kemp, R.A.; Takase, M.K. Experimental and Computational Studies of the Reaction of Carbon Dioxide with Pincer-Supported Nickel and Palladium Hydrides. *Organometallics* **2012**, *31*, 8225–8236. [CrossRef]
19. Stephens, P.J.; Devlin, F.J.; Chabalowski, C.F.; Frisch, M.J. Ab Initio Calculation of Vibrational Absorption and Circular Dichroism Spectra Using Density Functional Force Fields. *J. Phys. Chem.* **1994**, *98*, 11623–11627. [CrossRef]
20. Becke, A.D. Density-functional thermochemistry. III. The role of exact exchange. *J. Chem. Phys.* **1993**, *98*, 5648–5652. [CrossRef]
21. Lee, C.; Yang, W.; Parr, R.G. Development of the Colle-Salvetti correlation-energy formula into a functional of the electron density. *Phys. Rev. B Condens. Matter* **1988**, *37*, 785–789. [CrossRef] [PubMed]
22. Miehlich, B.; Savin, A.; Stoll, H.; Preuss, H. Results Obtained With The Correlation Energy Density Functionals Of Becke And Lee, Yang And Parr. *Chem. Phys. Lett.* **1989**, *157*, 200–206. [CrossRef]
23. Frisch, M.J.; Trucks, G.W.; Schlegel, H.B.; Scuseria, G.E.; Robb, M.A.; Cheeseman, J.R.; Scalmani, G.; Barone, V.; Petersson, G.A.; Nakatsuji, H.; et al. *Gaussian 16, Revision C.01*; Gaussian, Inc.: Wallingford, CT, USA, 2019.
24. Hay, P.J.; Wadt, W.R. Ab initio effective core potentials for molecular calculations. Potentials for K to Au including the outermost core orbitals. *J. Chem. Phys.* **1985**, *82*, 299–310. [CrossRef]
25. Couty, M.; Hall, M.B. Basis sets for transition metals: Optimized outer p functions. *J. Comput. Chem.* **1996**, *17*, 1359–1370. [CrossRef]
26. Check, C.E.; Faust, T.O.; Bailey, J.M.; Wright, B.J.; Gilbert, T.M.; Sunderlin, L.S. Addition of polarization and diffuse functions to the LANL2DZ basis set for p-block elements. *J. Phys. Chem. A* **2001**, *105*, 8111–8116. [CrossRef]
27. Hehre, W.J.; Ditchfield, R.; Pople, J.A. Self-Consistent Molecular-Orbital Methods. XII. Further Extensions of Gaussian-Type Basis Sets for Use in Molecular-Orbital Studies of Organic-Molecules. *J. Chem. Phys.* **1972**, *56*, 2257–2261. [CrossRef]
28. Hariharan, P.C.; Pople, J.A. The Influence of Polarization Functions on Molecular-Orbital Hydrogenation Energies. *Theor. Chim. Acta* **1973**, *28*, 213–222. [CrossRef]
29. Perdew, J.P. Density-functional approximation for the correlation energy of the inhomogeneous electron gas. *Phys. Rev. B Condens. Matter* **1986**, *33*, 8822–8824. [CrossRef]
30. Foresman, J.B.; Frisch, A. *Exploring Chemistry with Electronic Structure Methods*, 2nd ed.; Gaussian, Inc.: Pittsburgh, PA, USA, 1996.
31. Marenich, A.V.; Cramer, C.J.; Truhlar, D.G. Universal Solvation Model Based on Solute Electron Density and on a Continuum Model of the Solvent Defined by the Bulk Dielectric Constant and Atomic Surface Tensions. *J. Phys. Chem. B* **2009**, *113*, 6378–6396. [CrossRef]
32. Weigend, F.; Ahlrichs, R. Balanced basis sets of split valence, triple zeta valence and quadruple zeta valence quality for H to Rn: Design and assessment of accuracy. *Phys. Chem. Chem. Phys.* **2005**, *7*, 3297–3305. [CrossRef]
33. Andrae, D.; Häusermann, U.; Dolg, M.; Stoll, H.; Preuss, H. Energy-adjusted ab initio pseudopotentials for the second and third row transition elements. *Theor. Chim. Acta* **1990**, *77*, 123–141. [CrossRef]
34. Wiedner, E.S.; Chambers, M.B.; Pitman, C.L.; Bullock, R.M.; Miller, A.J.M.; Appel, A.M. Thermodynamic hydricity of transition metal hydrides. *Chem. Rev.* **2016**, *116*, 8655–8692. [CrossRef] [PubMed]
35. Ilic, S.; Alherz, A.; Musgrave, C.B.; Glusac, K.D. Thermodynamic and kinetic hydricities of metal-free hydrides. *Chem. Soc. Rev.* **2018**, *47*, 2809–2836. [CrossRef] [PubMed]
36. Liang, G.; Zhang, M.; Webster, C.E. Mechanistic Studies of Oxygen-Atom Transfer (OAT) in the Homogeneous Conversion of N_2O by Ru Pincer Complexes. *Inorganics* **2022**, *10*, 69. [CrossRef]
37. Grimme, S.; Antony, J.; Ehrlich, S.; Krieg, H. A consistent and accurate ab initio parametrization of density functional dispersion correction (DFT-D) for the 94 elements H-Pu. *J. Chem. Phys.* **2010**, *132*, 154104. [CrossRef]
38. Grimme, S.; Ehrlich, S.; Goerigk, L. Effect of the damping function in dispersion corrected density functional theory. *J. Comput. Chem.* **2011**, *32*, 1456–1465. [CrossRef]
39. Dunlap, B.I. Fitting the Coulomb potential variationally in Xα molecular calculations. *J. Chem. Phys.* **1983**, *78*, 3140–3142. [CrossRef]
40. Dunlap, B.I. Robust and variational fitting: Removing the four-center integrals from center stage in quantum chemistry. *J. Mol. Struct. THEOCHEM* **2000**, *529*, 37–40. [CrossRef]
41. Zhang, M.; Liang, G. Understanding the Sigmatropic Shifts of Cyclopenta-2,4-dien-1-yltrimethylsilane in its Diels—Alder Addition. *Org. Biomol. Chem.* **2021**, *19*, 1732–1737. [CrossRef]
42. Bader, R.F.W. Atoms in molecules. *Acc. Chem. Res.* **1985**, *18*, 9–15. [CrossRef]
43. Bader, R.F.W. *Atoms in Molecules: A Quantum Theory*; Oxford University Press: Oxford, UK, 1990.
44. Bader, R.F.W. A quantum theory of molecular structure and its applications. *Chem. Rev.* **1991**, *91*, 893–928. [CrossRef]
45. Casals-Sainz, J.L.; Fernández-Alarcón, A.; Francisco, E.; Costales, A.; Pendás, Á.M. Bond Order Densities in Real Space. *J. Phys. Chem. A* **2020**, *124*, 339–352. [CrossRef] [PubMed]
46. *Multiwfn*, Version 3.8; 2021. Available online: http://sobereva.com/multiwfn/ (accessed on 2 December 2021).

47. Lu, T.; Chen, F. Multiwfn: A multifunctional wavefunction analyzer. *J. Comput. Chem.* **2012**, *33*, 580–592. [CrossRef] [PubMed]
48. Humphrey, W.; Dalke, A.; Schulten, K. VMD: Visual molecular dynamics. *J. Mol. Graph.* **1996**, *14*, 33–38. [CrossRef]
49. *VMD*, Version 1.9.3; 2016. Available online: http://www.ks.uiuc.edu/Research/vmd/ (accessed on 4 December 2021).
50. Falivene, L.; Credendino, R.; Poater, A.; Petta, A.; Serra, L.; Oliva, R.; Scarano, V.; Cavallo, L. SambVca 2. A Web Tool for Analyzing Catalytic Pockets with Topographic Steric Maps. *Organometallics* **2016**, *35*, 2286–2293. [CrossRef]
51. *SambVca*, Version 2.1; 2019. Available online: https://www.molnac.unisa.it/OMtools/sambvca2.1/index.html (accessed on 12 November 2021).
52. Falivene, L.; Cao, Z.; Petta, A.; Serra, L.; Poater, A.; Oliva, R.; Scarano, V.; Cavallo, L. Towards the online computer-aided design of catalytic pockets. *Nat. Chem.* **2019**, *11*, 872–879. [CrossRef]
53. Poater, A.; Ragone, F.; Giudice, S.; Costabile, C.; Dorta, R.; Nolan, S.P.; Cavallo, L. Thermodynamics of N-Heterocyclic Carbene Dimerization: The Balance of Sterics and Electronics. *Organometallics* **2008**, *27*, 2679–2681. [CrossRef]
54. Poater, A.; Ragone, F.; Mariz, R.; Dorta, R.; Cavallo, L. Comparing the Enantioselective Power of Steric and Electrostatic Effects in Transition-Metal-Catalyzed Asymmetric Synthesis. *Chem. Eur. J.* **2010**, *16*, 14348–14353. [CrossRef]
55. Zhang, M.; Liang, G.; Xing, M. Theoretical Investigation of Hydrogen Bonds Assisted Tetradentate N4 Copper(I) Chloride and trans-1,2-Peroxodicopper Complexes. *Eur. J. Inorg. Chem.* **2021**, *2021*, 2194–2200. [CrossRef]
56. Witte, J.; Mardirossian, N.; Neaton, J.B.; Head-Gordon, M. Assessing DFT-D3 Damping Functions Across Widely Used Density Functionals: Can We Do Better? *J. Chem. Theory Comput.* **2017**, *13*, 2043–2052. [CrossRef]
57. Zhang, L.; An, K.; Wang, Y.; Wu, Y.-D.; Zhang, X.; Yu, Z.-X.; He, W. A Combined Computational and Experimental Study of Rh-Catalyzed C–H Silylation with Silacyclobutanes: Insights Leading to a More Efficient Catalyst System. *J. Am. Chem. Soc.* **2021**, *143*, 3571–3582. [CrossRef] [PubMed]
58. Zheng, D.; Wang, F. Performing Molecular Dynamics Simulations and Computing Hydration Free Energies on the B3LYP-D3(BJ) Potential Energy Surface with Adaptive Force Matching: A Benchmark Study with Seven Alcohols and One Amine. *ACS Phys. Chem. Au* **2021**, *1*, 14–24. [CrossRef] [PubMed]
59. Hazari, N.; Heimann, J.E. Carbon Dioxide Insertion into Group 9 and 10 Metal–Element σ Bonds. *Inorg. Chem.* **2017**, *56*, 13655–13678. [CrossRef] [PubMed]